

STEADY AND UNSTEADY TRANSONIC SMALL DISTURBANCE
ANALYSIS OF REALISTIC AIRCRAFT CONFIGURATIONS

John T. Batina
David A. Seidel
Robert M. Bennett
Herbert J. Cunningham
Samuel R. Bland
NASA Langley Research Center
Hampton, Virginia

Summary

A transonic unsteady aerodynamic and aeroelasticity code called CAP-TSD has been developed for application to realistic aircraft configurations. The name CAP-TSD is an acronym for Computational Aeroelasticity Program - Transonic Small Disturbance. The code permits the calculation of steady and unsteady flows about complete aircraft configurations for aeroelastic analysis in the flutter critical transonic speed range. The CAP-TSD code uses a time-accurate approximate factorization (AF) algorithm for solution of the unsteady transonic small-disturbance potential equation. The paper gives an overview of the CAP-TSD code development effort and reports on recent algorithm modifications. The algorithm modifications include: an Engquist-Osher (E-O) type-dependent switch to treat regions of supersonic flow, extension of the E-O switch for second-order spatial accuracy, nonisentropic effects to treat strong-shock cases, nonreflecting far field boundary conditions for unsteady applications, and several modifications to accelerate convergence to steady-state. Calculations are presented for several configurations including the General Dynamics one-ninth scale F-16C aircraft model to evaluate the algorithm modifications. The modifications have significantly improved the stability of the AF algorithm and hence the reliability of the CAP-TSD code in general. Calculations are also presented from a flutter analysis of a 45° sweptback wing which agree well with the experimental data. The paper presents descriptions of the CAP-TSD code and algorithm details along with results and comparisons which demonstrate the stability, accuracy, efficiency, and utility of CAP-TSD.

Introduction

Presently, considerable research is being conducted to develop finite-difference computer codes for calculating transonic unsteady aerodynamics for aeroelastic applications.¹ These computer codes are being developed to provide accurate methods of calculating unsteady airloads for the prediction of aeroelastic phenomena such as flutter and divergence. For example, the CAP-TSD² unsteady transonic small-disturbance (TSD) code was recently developed for transonic aeroelastic analyses of complete aircraft configurations. The name CAP-TSD is an acronym for Computational Aeroelasticity Program - Transonic Small Disturbance. The new code permits the calculation of unsteady flows about complete aircraft for aeroelastic analysis in the flutter critical transonic speed range. The code can treat configurations with arbitrary combinations of lifting surfaces and bodies including canard, wing, tail, control surfaces, tip launchers, pylons, fuselage, stores, and nacelles. Steady and unsteady pressure comparisons were presented in Refs. 2 and 3 for numerous cases which

demonstrated the geometrical applicability of CAP-TSD. These calculated results were generally in good agreement with available experimental pressure data which validated CAP-TSD for multiple component applications with mutual aerodynamic interference effects. Preliminary aeroelastic applications of CAP-TSD were presented in Ref. 4 for a simple well-defined wing case. The case was selected as a first step toward performing aeroelastic analyses for complete aircraft configurations. The calculated flutter boundaries compared well with the experimental data for subsonic, transonic, and supersonic freestream Mach numbers, which gives confidence in CAP-TSD for aeroelastic prediction.

The CAP-TSD code uses a time-accurate approximate factorization (AF) algorithm recently developed by Batina⁵ for solution of the unsteady TSD equation. The AF algorithm involves a Newton linearization procedure coupled with an internal iteration technique. In Ref. 5, the algorithm was shown to be efficient for application to steady or unsteady transonic flow problems. It can provide accurate solutions in only several hundred time steps, yielding a significant computational cost savings when compared to alternative methods. For reasons of practicality and affordability, an efficient algorithm and a fast computer code are requirements for realistic aircraft applications.

Recently, several algorithm modifications have been made which have improved the stability of the AF algorithm and the accuracy of the results.^{6,7} These algorithm modifications include: (1) an Engquist-Osher (E-O) type-dependent switch to more accurately and efficiently treat regions of supersonic flow, (2) extension of the E-O switch for second-order-accurate spatial differencing in supersonic regions to improve the accuracy of the results, (3) nonisentropic effects to more accurately treat cases with strong shocks, (4) nonreflecting far field boundary conditions for more accurate unsteady applications, and (5) several modifications which accelerate convergence to steady-state. The work has been a major research activity over the past two years within the Unsteady Aerodynamics Branch at NASA Langley Research Center. The purpose of the paper is to give an overview of the CAP-TSD code development effort and report on the recent algorithm changes and code improvements. The paper documents these developments and presents results which demonstrate the capability.

Symbols

b_0	reference length, $c_r/2$
c	airfoil chord
c_{l_α}	unsteady lift-curve slope
c_r	wing reference chord
C_p	pressure coefficient
k	reduced frequency, $\omega c_r/2U$
M	freestream Mach number
$NSUP$	number of supersonic points
$q_i(t)$	generalized displacement for mode i
R	residual
t	time, nondimensionalized by freestream speed and wing reference chord
U	freestream speed
α	instantaneous angle of attack
α_0, α_1	mean angle of attack and amplitude of pitch oscillation, respectively

γ	ratio of specific heats
Δt	nondimensional time step
$\bar{\eta}$	fractional semispan
μ	ratio of wing mass to mass of air in the truncated cone that encloses the wing
ρ	freestream flow density
ϕ	disturbance velocity potential
ω	angular frequency
ω_α	natural frequency of the first torsion mode

Subscripts

t	tail
w	wing

Transonic Small-Disturbance Equation

The flow is assumed to be governed by the general frequency modified TSD potential equation which may be written as

$$M^2 (\phi_t + 2\phi_x)_t = [(1 - M^2)\phi_x + F\phi_x^2 + G\phi_y^2]_x + (\phi_y + H\phi_x\phi_y)_y + (\phi_z)_z \quad (1)$$

Several choices are available for the coefficients F, G, and H depending upon the assumptions used in deriving the TSD equation. For transonic applications, the coefficients are herein defined as

$$F = -\frac{1}{2}(\gamma + 1)M^2, \quad G = \frac{1}{2}(\gamma - 3)M^2, \quad H = -(\gamma - 1)M^2 \quad (2)$$

The linear potential equation is recovered by simply setting F, G, and H equal to zero.

Approximate Factorization Algorithm

A time-accurate approximate factorization algorithm was developed⁵ to solve the unsteady TSD equation. In this section, the AF algorithm is briefly described.

General Description

The AF algorithm consists of a Newton linearization procedure coupled with an internal iteration technique. For unsteady flow calculations, the solution procedure involves two steps. First, a time linearization step (described below) is performed to determine an estimate of the potential field. Second, internal iterations are performed to provide time-accurate modeling of the flow field. Specifically, the TSD equation is written in general form as

$$R(\phi^{n+1}) = 0 \quad (3)$$

where ϕ^{n+1} represents the unknown potential field at time level (n+1). The solution to Eq. (3) is then given by the Newton linearization of Eq. (3) about ϕ^*

$$R(\phi^*) + \left(\frac{\partial R}{\partial \phi}\right)_{\phi=\phi^*} \Delta\phi = 0 \quad (4)$$

In Eq. (4), ϕ^* is the currently available value of ϕ^{n+1} and $\Delta\phi = \phi^{n+1} - \phi^*$. During convergence of the iteration procedure, $\Delta\phi$ will approach zero so that the solution will be given by $\phi^{n+1} = \phi^*$. In general, only one or two iterations are required to achieve acceptable convergence. For steady flow calculations, iterations are not used since time accuracy is not necessary when marching to steady state.

Mathematical Formulation

The AF algorithm is formulated by first approximating the time-derivative terms by second-order-accurate finite-difference formulae. The TSD equation is rewritten by substituting $\phi = \phi^* + \Delta\phi$ and neglecting squares of derivatives of $\Delta\phi$ (which is equivalent to applying Eq. (4) term by term). The resulting equation is then rearranged and the left-hand side is approximately factored into a triple product of operators yielding

$$L_\xi L_\eta L_\zeta \Delta\phi = -\sigma R(\phi^*, \phi^n, \phi^{n-1}, \phi^{n-2}) \quad (5)$$

where the operators L_ξ , L_η , L_ζ and residual R were derived and presented in Ref. 5. In Eq. (5) σ is a relaxation parameter which is normally set equal to 1.0. To accelerate convergence to steady-state, the residual R may be over-relaxed using $\sigma > 1$. Equation (5) is solved using three sweeps through the grid by sequentially applying the operators L_ξ , L_η , L_ζ as

$$\xi - \text{sweep: } L_\xi \bar{\Delta\phi} = -\sigma R \quad (6a)$$

$$\eta - \text{sweep: } L_\eta \bar{\Delta\phi} = \bar{\Delta\phi} \quad (6b)$$

$$\zeta - \text{sweep: } L_\zeta \bar{\Delta\phi} = \bar{\Delta\phi} \quad (6c)$$

Further details of the algorithm development and solution procedure may be found in Ref. 5.

Flow-Tangency Boundary Conditions

The flow tangency boundary conditions are imposed along the mean plane of the respective lifting surfaces and the wakes are assumed to be planar extensions from the trailing edges to the downstream boundary of the finite-difference grid. The numerical implementation of these conditions² allows for coplanar as well as non-coplanar combinations of horizontal (canard, wing, horizontal tail, launchers) and vertical (pylons, vertical tail) surfaces. Bodies such as the fuselage, stores, and nacelles are treated using simplified boundary conditions on a prismatic surface rather than on the true surface.² The method is consistent with the small-disturbance approximation and treats bodies with sufficient accuracy to obtain the correct global effect on the flow field without the use of special grids or complicated coordinate transformations. This type of modeling is similar to that of Boppe and Stern,⁸ where good agreement was shown in comparison with experimental data for configurations with a fuselage and flow-through nacelles.

Time-Linearization Step

An initial estimate of the potentials at time level $(n+1)$ is required to start the iteration process. This estimate is provided by performing a time-linearization calculation. The equations governing the time-linearization step are derived in a similar fashion as the equations for iteration. The only difference is that the equations are formulated by linearizing about time level (n) rather than the iterate level $(*)$.

Algorithm Improvements

Engquist-Osher Type-Dependent Switch

Algorithms based on the TSD equation typically use central differencing in regions of subsonic flow and upwind differencing in regions of supersonic flow. This, of course, allows for the correct numerical description of the physical domain of dependence. The original CAP-TSD code of Ref. 2 used the Murman⁹ type-dependent switch to change the spatial differencing. The Murman switch, however, admits nonphysical expansion shocks as a part of the solution and has been shown to be less stable than monotone methods.^{10,11} For example, unsteady results for a NACA 64A006 airfoil were presented in Ref. 11 which demonstrated an order of magnitude increase in time step using a monotone algorithm. Therefore, an Engquist-Osher (E-O) monotone switch, similar to that of Ref. 10, has been incorporated within the AF algorithm of the CAP-TSD code.⁶ The E-O switch is based on sonic reference conditions and does not admit expansion shocks as part of the solution. Use of the E-O switch also generally increases computational efficiency because of the larger time steps which may be taken.

Second-Order-Accurate Spatial Differencing

Most TSD algorithms are only first-order-accurate spatially in regions of supersonic flow. This is due to the first-order upwind differencing that is typically used to treat these regions. Use of second-order upwind differencing has been shown to improve the accuracy of the solution while

retaining the numerical stability of the first-order method.¹² Consequently, the E-O type dependent switch of the AF algorithm has been extended for second-order spatial accuracy in supersonic regions of the flow.⁶ Comparisons of results obtained using first-order and second-order differencing, to be presented, demonstrate the improved accuracy of the second-order method.

Entropy and Vorticity Effects

A serious limitation of the potential flow codes, in general, is the inability to accurately treat cases with strong shock waves. For these cases, the isentropic potential formulation typically overpredicts the shock strength and locates the shock too far aft in comparison with experiment. In fact, it is fairly well known that potential theory predicts non-unique steady-state solutions^{13,14} for narrow ranges of Mach number and angle of attack. Simple modifications to potential theory, however, have been shown to eliminate the nonuniqueness problem and consequently provide solutions which more accurately simulate those computed using the Euler equations.¹⁵⁻¹⁸ These modifications include the effects of shock generated entropy and they require only minor changes to existing computer codes.

Rotational effects may also become important when strong shock waves are present in the flow. For example, vorticity is generated by shock waves due to the variation of entropy along the shock. Potential theory, of course, does not account for these effects because of the irrotationality assumption necessary for the existence of a velocity potential. For these cases the Euler equations are generally required to accurately model the flow. Recently, however, simple modifications to potential theory have been developed to model rotational effects.^{19,20} These modifications involve a velocity decomposition originally suggested by Clebsch.²¹ In this model, the velocity vector is decomposed into a potential part and a rotational part. For most applications of interest to the aeroelastician, the rotational part occurs only in the region downstream of shocks. Therefore, the potential part can be obtained throughout most of the flow field using an existing potential flow code. The rotational part can then either be incorporated as a source term in the governing equation or as a modification to the fluxes, by making simple changes to the solution procedure. These changes consequently include the effects of shock generated vorticity as well as entropy and require relatively straightforward modifications to existing potential codes.

Entropy and vorticity modifications to TSD theory have been implemented within the AF algorithm of the CAP-TSD code as described in Ref. 7. These modifications include: (1) an alternative streamwise flux in the TSD equation which was derived by an asymptotic expansion of the Euler equations,²² (2) a modified velocity vector which is the sum of potential and rotational parts which in turn modifies the streamwise flux, and (3) the calculation and convection of entropy throughout the flow field. The modified code includes the effects of entropy and vorticity while retaining the relative simplicity and cost efficiency of the TSD formulation. Results obtained including these effects, to be presented, clearly demonstrate the improved accuracy of the AF algorithm.

Nonreflecting Far Field Boundary Conditions

For unsteady applications, the far field boundary conditions can have a significant influence on the accuracy of the solution. Steady-state boundary conditions are inadequate for unsteady

calculations, since disturbances reaching the boundaries are reflected back into the computational domain. These reflected disturbances can propagate into the near field and thus produce inaccurate results. One solution to this problem is to locate the grid boundaries far away to minimize the effect of the boundary conditions. This is generally not an acceptable remedy because of the higher computational cost which results from an increased number of grid points required to discretize a larger computational domain. The more appropriate solution is the use of nonreflecting far field boundary conditions which absorb most of the waves that are incident on the boundaries and consequently allow the use of smaller computational grids.²³ Nonreflecting boundary conditions similar to those of Whitlow²³ have been incorporated within the CAP-TSD code.⁶ These boundary conditions are consistent with the AF solution procedure and are described in more detail in Ref. 6. Results obtained with and without the nonreflecting boundary conditions are presented which demonstrate their effectiveness.

Steady-State Convergence Acceleration

Finally, several algorithm changes have been made to accelerate convergence to steady-state.⁶ Besides the E-O switch, these changes include: (1) deletion of the time-dependent terms from the residual of the AF algorithm, (2) deletion of all of the time-derivatives of the TSD equation, and (3) over-relaxation of the residual. The effects of these modifications on the steady-state convergence are demonstrated in the results presented herein.

Aeroelastic Solution

In this section the aeroelastic computational procedures are described including the equations of motion and the time-marching solution.

Equations of Motion

The aeroelastic equations of motion are based on a right-hand orthogonal coordinate system with the x-direction defined as positive downstream and the z-direction positive upward.⁴ The presentation herein is limited to the case of an isolated wing with motion in the z-direction from an undisturbed position in the $z = 0$ plane. The equations of motion may be written as

$$M\ddot{q} + C\dot{q} + Kq = Q \quad (7)$$

where q is a vector of generalized displacements, M is the generalized mass matrix, C is the damping matrix, and K is the stiffness matrix. In Eq. (7) Q is the vector of generalized aerodynamic forces defined by

$$Q_i = \frac{\rho U^2}{2} c_r^2 \int_s h_i \frac{\Delta p}{\rho U^2/2} \frac{dS}{c_r^2} \quad (8)$$

where Δp is the lifting pressure which is weighted by the mode h_i . The equations of motion (Eq. (7)) are solved by time-integration by first rewriting Eq. (7) as

$$\ddot{\mathbf{q}} = -\mathbf{M}^{-1} \mathbf{K} \mathbf{q} - \mathbf{M}^{-1} \mathbf{C} \dot{\mathbf{q}} + \mathbf{M}^{-1} \mathbf{Q} \quad (9)$$

Time-Marching Solution

The aeroelastic solution procedure for integrating Eq. (9) is similar to that described by Edwards, et al.²⁴ Reference 24 describes for a two-dimensional, two-degree-of-freedom system an aeroelastic solution in terms of a state equation formulation. By a parallel formulation, a linear state equation is developed from Eq. (9) which is solved numerically using the modified state-transition matrix integrator of Ref. 24. This integrator was shown to be superior to six alternative structural integration algorithms.²⁵

For aeroelastic analysis, two steps are generally required in performing the calculations. In the first step, the steady-state flow field is calculated to account for wing thickness, camber, and mean angle of attack thus providing the starting flow field for the aeroelastic analysis. The second step is to prescribe an initial disturbance to begin the structural integration. Disturbance velocities in one or more modes, rather than displacements, have been found to be distinctly superior in avoiding nonphysical, strictly numerical transients and their possible associated instabilities. In determining a flutter point, the freestream Mach number M and the associated freestream speed U are usually held fixed. A judiciously chosen value of the dynamic pressure $\rho U^2/2$ is used to compute the free decay transients. These resulting transients of the generalized coordinates are analyzed for their content of damped or growing sine-waves, with the rates of growth or decay indicating whether the dynamic pressure is above or below the flutter value. This analysis then indicates whether to increase or decrease the value of dynamic pressure in subsequent runs to determine a neutrally stable result.

CAP-TSD Code

The AF algorithm is the basis of the CAP-TSD code for transonic unsteady aerodynamic and aeroelastic analysis of realistic aircraft configurations. The present capability has the option of half-span modeling for symmetric cases or full-span modeling to allow the treatment of antisymmetric mode shapes, fuselage yaw, or unsymmetric configurations such as an oblique wing or unsymmetric wing stores. In the present coding of the AF algorithm, the time derivatives are implemented for variable time stepping to allow for step-size cycling to accelerate convergence to steady state. Also, since the L_ξ , L_η , and L_ζ operators only contain derivatives in their respective coordinate directions, all three sweeps of the solution procedure have been fully vectorized.

Results and Discussion

Results are presented for several configurations to demonstrate and evaluate the modifications to the AF algorithm of the CAP-TSD code. Calculations are also presented from a flutter analysis of a

45° sweptback wing to assess the aeroelastic capability of the code.

Flat Plate Airfoil Results

Unsteady results were obtained for a flat plate airfoil at $M = 0.85$ to test the nonreflecting far field boundary conditions.⁶ The flat plate airfoil was selected to allow direct comparison of results with the exact kernel function method of Bland.²⁶ The boundary conditions were tested by computing the lift coefficient due to the airfoil pitching about the quarter chord. Such unsteady forces are typically determined by calculating several cycles of forced harmonic oscillation with the last cycle providing the estimate of the forces. Alternatively, the forces may be obtained indirectly from the response due to a smoothly varying exponentially shaped pulse.²⁷ In this procedure, the airfoil is given a small prescribed pulse in a given mode of motion (in this case pitching) and the aerodynamic transients calculated. The harmonic response is obtained by a transfer-function analysis using fast Fourier transforms. Use of the pulse transfer-function technique gives considerable detail in the frequency domain with a significant reduction in cost over the alternative method of calculating multiple oscillatory responses. For the flat plate airfoil, pulse transient calculations were performed using 1024 time steps with $\Delta t = 0.2454$. The amplitude of the pulse was 0.5° . The grid extended 25 chordlengths above and below the airfoil, and 20 chordlengths upstream and downstream of the airfoil. Parallel results were obtained using reflecting (steady-state) and nonreflecting far field boundary conditions as shown in Fig. 1. The results are plotted as real and imaginary components of the unsteady lift-curve slope c_{l_α} as a function of reduced frequency k . Computations using the reflecting boundary conditions, shown in Fig. 1(a) produce oscillations in both the real and imaginary parts for $0 < k < 0.2$. The oscillations are produced by reflected disturbances which propagate back into the near field and contaminate the solution. When the calculation was repeated using the nonreflecting boundary conditions, shown in Fig. 1(b), the oscillations no longer occur since the boundary conditions absorb most of the disturbances that are incident on the grid boundaries. Furthermore, these results are in excellent agreement with calculations from the kernel function method of Ref. 26.

F-5 Wing Results

Calculations were next performed for the F-5 wing²⁸ to assess the algorithm modifications⁶ to CAP-TSD. The F-5 wing has an aspect ratio of 3.16, a leading edge sweep angle of 31.9° , and a taper ratio of 0.28. The airfoil section of the wing is a modified NACA 65A004.8 airfoil which has a drooped nose and is symmetric aft of 40% chord. The F-5 calculations were performed using a constant step size for a total of 500 steps. The freestream Mach number was selected as 0.9 and the wing was at 0° angle of attack. The results were obtained to study the steady-state convergence characteristics of the modified AF algorithm. The results are presented in the form of convergence histories and the number of supersonic (NSUP) points versus the iteration number.

In the original AF algorithm of Ref. 5, the Murman type-dependent switch was used. Results obtained using the unmodified code are presented in Fig. 2. The steady-state convergence is shown in Fig. 2(a); the number of supersonic points (NSUP) normalized by the final value are shown in Fig. 2(b). For aeroelastic analysis where airloads are required rather than pressures, the solution is considered to be converged to engineering accuracy when a three to four order-of-magnitude reduction in the solution error is obtained. The "error" in the convergence history, as defined

herein, is the ratio of the maximum $|\Delta\phi|$ after n iterations to the maximum $|\Delta\phi|$ in the initial solution (first iteration). Two sets of results are plotted corresponding to two values of step size, $\Delta t = 0.1$ and 0.5 . For $\Delta t = 0.1$, the rate of convergence is slow and the number of supersonic points oscillates about the final value. Increasing the step size to $\Delta t = 0.5$ improves the rate of convergence and the oscillations in NSUP are significantly damped. The results for $\Delta t = 0.5$ also indicate that the number of supersonic points is initially more than four and one-half times the final value and that "spikes" begin to appear in the convergence history after 150 steps. These spikes, which represent a numerical instability, are due to a large transient caused by the impulsive start from a uniform stream using a large step size. If the calculations were started with a smaller step size, and then the step size increased to the larger value, the numerical instability can be avoided. Also, as shown in Refs. 2 and 5, the step size may be cycled through very large values such as $\Delta t = 5.0$ to achieve faster convergence to steady-state.

The F-5 calculations with $\Delta t = 0.5$ were then repeated with the E-O switch replacing the Murman switch. These results are labeled "unsteady algorithm" in Fig. 3. The curves are almost identical to the $\Delta t = 0.5$ curves of Fig. 2 except that the spikes in the convergence history are absent. The E-O switch is more robust than the Murman switch and thus the calculation remains stable. Furthermore, the rate of convergence to steady-state could be increased by deleting the time derivatives in the residual, over-relaxing the residual, or deleting all of the time derivatives in the TSD equation.⁶ By deleting all of the time derivatives, the algorithm solves the steady TSD equation and is therefore referred to as the "steady algorithm." Results obtained using this algorithm are compared with the unsteady algorithm results in Fig. 3. The convergence history computed using the steady algorithm is monotonically decreasing and very smooth in comparison with the unsteady algorithm convergence history. The steady algorithm solution converges faster and does not produce the large initial overprediction of NSUP that is characteristic of the unsteady algorithm. The number of supersonic points converges rapidly to within 2% of its final value in only approximately 25 steps. Over-relaxing the residual of the steady algorithm also further accelerates the convergence to steady-state (not shown).

ONERA M6 Wing Results

To test the accuracy of the modified CAP-TSD algorithm,⁶ calculations were performed for the ONERA M6 wing.²⁹ The M6 wing has an aspect ratio of 3.8, a leading edge sweep angle of 30° , and a taper ratio of 0.562. The airfoil section of the wing is the ONERA "D" airfoil which is a 10% maximum thickness-to-chord ratio conventional section. The freestream Mach number was selected as $M = 0.84$ and the wing was at 3.06° angle of attack. These conditions were chosen for comparison with the tabulated experimental pressure data of Ref. 29. This rather well-known case is a very challenging one, especially for a TSD code, because of the complex double shock wave which occurs on the upper surface of the wing.

Steady-state calculations were performed for the M6 wing by using the AF algorithm with the E-O switch. The results were obtained by cycling the step size through values as large as $\Delta t = 2.0$ for a total of 500 steps. This relatively large step size corresponds to two root chords of travel per time step. A comparison of the resulting CAP-TSD pressures with the experimental pressure data is given in Fig. 4 for $\bar{\eta} = 0.44$. The data indicate that there is a relatively weak highly swept supersonic-to-supersonic shock wave which forms forward near the leading edge. The primary

supersonic-to-subsonic shock which occurs in the midchord region of the wing, coalesces with the first shock in the spanwise direction. Outboard toward the tip, the two shocks merge to form a single supersonic-to-subsonic shock wave. The CAP-TSD results obtained using first-order-accurate differencing in supersonic regions are in fairly good agreement with the data in predicting the overall pressure levels, although differences occur in the regions of the shocks. In general, the leading-edge suction peak is well predicted but the supersonic-to-supersonic shock is smeared. When the calculation was repeated using the second-order-accurate spatial differencing, a significant improvement was obtained in the accuracy of the results. The comparisons in Fig. 4 show that the supersonic-to-supersonic shock is much more sharply captured by the second-order method and consequently the calculated pressures are now in very good agreement with the experimental data. Calculations were also performed for the M6 wing using the original algorithm with the Murman switch. These calculations were unsuccessful because of a numerical instability which was produced by the highly expanded flow about the leading edge of the wing.

An unsteady calculation was also performed for the M6 wing at $M = 0.84$, to investigate the robustness of the modified algorithm for time-dependent applications. In this demonstration calculation, the wing was forced to oscillate in pitch about a line perpendicular to the root at the root midchord. The amplitude of the motion was 2° peak-to-peak about the mean angle of attack of $\alpha_0 = 3.06^\circ$. The reduced frequency was selected as $k = 0.1$ and only 300 steps per cycle of motion were used. This corresponds to a step size of $\Delta t = 0.1047$. Three cycles of motion were computed to obtain a periodic solution. Unsteady pressure distributions, obtained using first-order and second-order accurate supersonic differencing, are shown in Fig. 5 at the maximum pitch angle ($\alpha = 4.06^\circ$) for $\bar{\eta} = 0.44$. Similar to the steady-state results, these pressure comparisons illustrate that the supersonic-to-supersonic shock is more sharply captured by the second-order method. Further instantaneous pressure distributions at two points during the third cycle of motion are shown in Fig. 6 for five span stations along the wing. Pressures at the wing maximum angle of attack ($\alpha = 4.06^\circ$) and pressures at the wing minimum angle of attack ($\alpha = 2.06^\circ$) are both presented in the figure. As the wing pitches up, the shocks move aft and the supersonic-to-subsonic shock grows in strength. As the wing pitches down, the shocks move forward and the supersonic-to-supersonic shock is more sharply defined. For this case, both of the shocks oscillate over approximately 10% of the chord during a cycle of motion. Also, the supersonic-to-supersonic shock at $\bar{\eta} = 0.80$ periodically appears and disappears during a cycle of motion. The results illustrate the large shock motions that the modified AF algorithm is capable of computing. The improved algorithm captures the shocks sharply and is sufficiently robust to compute this complex unsteady flow using only 300 steps per cycle of motion.

To test the entropy and vorticity modifications to TSD theory,⁷ further calculations were performed for the M6 wing. Results were obtained at the freestream Mach number of $M = 0.92$ with the wing at 0° mean angle of attack. These conditions correspond to an AGARD test case for assessment of inviscid flow field methods³⁰ and were selected for comparison with the tabulated Euler results of Rizzi contained therein. Calculations were performed using: (a) unmodified TSD theory and (b) TSD with entropy and vorticity effects. Steady pressure distributions along three span stations ($\bar{\eta} = 0.08, 0.47$, and 0.82) of the wing are presented in Fig. 7 from both solutions. For this steady-state case, the flow is symmetric about the wing with shocks on the upper and lower surfaces. As shown in Fig. 7(a), the results from the unmodified TSD theory compare well with the Euler results in predicting the leading-edge suction peak and the overall pressure levels. However, the shock is located too far aft and is too strong outboard near the tip (at $\bar{\eta} = 0.82$, for example), in comparison with the Euler calculation. When the entropy and vorticity modifications are included in

the calculation, the shock is displaced forward from the previous solution, as shown in Fig. 7(b). Here the shock location and shock strength are in very good agreement with the Euler results at all three span stations on the wing. Consequently, the steady pressure distributions from the modified TSD theory now compare very well with the Euler pressures.

General Dynamics F-16C Aircraft Model Results

Results were also obtained for the General Dynamics F-16C aircraft model³¹ to investigate application of the modified algorithm to a realistic aircraft configuration.⁶ Shown in Fig. 8 are the F-16C components that are modeled using CAP-TSD. The F-16C is modeled using four lifting surfaces and two bodies. The lifting surfaces include: (1) the wing with leading and trailing edge control surfaces, (2) the launcher, (3) a highly swept strake, aft strake, and shelf surface, and (4) the horizontal tail. The bodies include: (1) the tip missile, and (2) the fuselage. In these calculations, the freestream Mach number was $M = 0.9$ and the F-16C aircraft was at 2.38° angle of attack. Also, the leading-edge control surface of the wing was deflected upwards 2° for comparison with the experimental steady pressure data of Ref. 32. Furthermore, the calculations were performed on a grid which conforms to the leading and trailing edges of the lifting surfaces and contains 324,000 points. Since the grid is Cartesian, it was relatively easy to generate, even for such a complex configuration as the F-16C aircraft. Also, the calculations required only about 0.88 CPU seconds per time step and thirteen million words of memory on the CDC VPS-32 computer at NASA Langley Research Center.

Steady-state calculations were performed for the F-16C aircraft using the AF algorithm with the E-O and Murman switches. The E-O results were obtained using both the first-order and second-order accurate supersonic differencing. Steady pressure comparisons are given in Fig. 9 for three span stations of the wing and one span station of the tail. Both sets of E-O results are presented for comparison with the experimental data. The results obtained using the Murman switch were originally published in Ref. 2. These results are identical to plotting accuracy with the first-order E-O results, and therefore are not shown. The steady pressure comparisons indicate that there is a moderately strong shock wave on the upper surface of the wing and the CAP-TSD pressures agree well with the experimental pressures. For the tail, the flow is predominantly subcritical and the calculated results again agree well with the data. Comparison of pressures computed using first-order and second-order accurate supersonic differencing shows very small differences. The largest difference, for example, occurs on the wing at $\bar{\eta}_w = 0.79$ where the second-order calculation predicts a slightly stronger shock.

Unsteady results were also obtained for the F-16C aircraft to investigate the robustness of the modified algorithm for realistic-aircraft time-dependent applications. For simplicity, the calculation was performed for a rigid pitching motion where the entire aircraft was forced to oscillate about the model moment reference axis at a reduced frequency of $k = 0.1$. The oscillation amplitude was chosen as $\alpha_1 = 1.5^\circ$ which is three times the value used to obtain similar results presented in Ref. 2. Three cycles of motion were computed using 300 steps per cycle of motion corresponding to $\Delta t = 0.1047$. Calculations were performed using both the Murman and E-O switches. The solution using the original algorithm with the Murman switch, however, was numerically unstable for this case as shown in Fig. 10. Instantaneous pressure distributions at time steps 94 and 95 are plotted in the figure, computed using the Murman (Fig. 10(a)) and E-O (Fig. 10(b)) switches. The numerical instability begins in the region of the launcher/tip-missile where

the grid spacing is smallest. Figure 10(a) shows the instability in the form of an oscillation in the wing upper surface pressure distribution at $\bar{\eta}_w = 0.94$ from approximately 30% to 60% chord. The program subsequently failed during step 96 which is 21 steps after the maximum pitch angle in the first cycle of motion. The calculation involving the modified algorithm (E-O switch with the first-order accurate supersonic differencing) is stable, however, as shown in Fig. 10(b). Here the pressure distributions for steps 94 and 95 are very similar and the calculation proceeds with no difficulty. In fact, the modified AF algorithm with the E-O switch is numerically stable for this case with either the first-order or second-order supersonic differencing.

Unsteady pressure distributions along the wing and tail during the third cycle of motion are shown in Fig. 11, computed using the E-O switch with the second-order accurate supersonic differencing. Two sets of calculated pressures are presented corresponding to the aircraft at the maximum ($\alpha = 3.88^\circ$) and minimum ($\alpha = 0.88^\circ$) pitch angles. Comparison of the results indicates that large changes in pressure occur along the upper and lower surfaces of the wing as the aircraft oscillates in pitch. For example, the shock on the wing upper surface oscillates over more than 10% of the chord during a cycle of motion. Also, the shock is approximately twice as strong at the maximum pitch angle as it is at the minimum pitch angle. For the tail, the changes in the pressure distributions due to aircraft pitching are relatively very small in comparison with the changes in wing pressures, as further shown in Fig. 11. The tail is located considerably aft of the pitch axis and thus its motion is plunge dominated which results in much smaller airloads for the low value of k considered.

Wing Flutter Results

To assess the CAP-TSD code for flutter applications, a simple well-defined wing case was selected as a first step toward performing aeroelastic analyses for complete aircraft configurations.⁴ The wing being analyzed is a semispan wind-tunnel-wall-mounted model that has a quarter-chord sweep angle of 45° , a panel aspect ratio of 1.65, and a taper ratio of 0.66.³³ The wing is a proposed AGARD standard aeroelastic configuration which was tested in the Transonic Dynamics Tunnel (TDT) at NASA Langley Research Center.³⁴ A planview of the wing is shown in Fig. 12. The wing has a NACA 65A004 airfoil section and was constructed of laminated mahogany. In order to obtain flutter for a wide range of Mach number and density conditions in the TDT, holes were drilled through the wing to reduce its stiffness. To maintain the aerodynamic shape of the wing, the holes were filled with a rigid foam plastic. A photograph of the model mounted in the TDT is shown in Fig. 13. The wing is being modeled structurally using the first four natural vibration modes which are illustrated in Figs. 14 and 15. Figure 14 shows oblique projections of the natural modes while Fig. 15 shows the corresponding deflection contours. These modes which are numbered 1 through 4 represent first bending, first torsion, second bending, and second torsion, respectively, as determined by a finite element analysis. The modes have natural frequencies which range from 9.6 Hz for the first bending mode to 91.54 Hz for the second torsion mode.

Flutter calculations were performed for the 45° sweptback wing using CAP-TSD to assess the code for aeroelastic applications. Two sets of results are presented corresponding to: (1) using the linear potential equation ($F = G = H = 0$) and modeling the wing aerodynamically as a flat plate (zero thickness) and (2) using the complete (nonlinear) TSD equation and including wing thickness. The first set of results allows for direct comparison with parallel linear theory calculations performed using the FAST subsonic kernel function program.³⁵ The second set of results more accurately

models the wing geometry as well as the flow physics. All of the results are compared with the experimental flutter data of Ref. 34 which spans the range, $0.338 \leq M \leq 1.141$.

Comparisons of flutter characteristics from the linear calculations with the experimental data are given in Fig. 16. Plots of flutter speed index (defined as $U/(b_0 \omega_\alpha \sqrt{\mu})$) and nondimensional flutter frequency (defined as ω/ω_α) as functions of freestream Mach number, are shown in Figs. 16(a) and 16(b), respectively. The experimental flutter data defines a typical transonic flutter "dip" with the bottom near $M = 1.0$ for this case. (Note that these results are shown with an expanded scale.) The bottom of the dip in flutter speed index (Fig. 16(a)) was defined by the approach to the $M = 1.072$ flutter point during the wind tunnel operation. Results from the CAP-TSD (linear) code are presented at twelve values of M covering the entire Mach number range over which the flutter data was measured. Results from the FAST program are presented for the limited range $0.338 \leq M \leq 0.96$ since the method is restricted to subsonic freestreams. Overall, the linear CAP-TSD results compare well with the experimental data for subsonic as well as supersonic Mach numbers. Note that the subsonic FAST results are also in good agreement with the data. Such a result is not unexpected for this very thin wing of moderate sweep and taper at zero angle of attack. It does indicate that the wing properties are well-defined for benchmark purposes.

In the subsonic Mach number range, the CAP-TSD and FAST calculations predict a slightly unconservative flutter speed, except at $M = 0.338$, by as much as 2% (Fig. 16(a)), and a higher flutter frequency (Fig. 16(b)) in comparison with the experimental data. In general though, the linear CAP-TSD results agree well with the FAST results in both flutter speed and frequency. The good agreement in this three-way correlation between experiment, linear theory, and CFD flutter results gives confidence in the CAP-TSD code for flutter prediction.

Comparisons of flutter characteristics from the linear and nonlinear CAP-TSD calculations with the experimental data are given in Fig. 17. Figure 17(a) shows flutter speed index versus Mach number and Fig. 17(b) shows nondimensional flutter frequency versus Mach number. Three flutter points are plotted from the nonlinear CAP-TSD calculations corresponding to $M = 0.678, 0.901$, and 0.96 . Comparisons between the two sets of CAP-TSD results show differences due to wing thickness and nonlinear effects. With increasing Mach number these differences become larger. For example, at $M = 0.678, 0.901$, and 0.96 , the flutter speed index decreased by 1%, 5%, and 19%, respectively, as shown in Fig. 17(a). Similar decreases also occur in the flutter frequency (Fig. 17(b)). The decrease in flutter speed at $M = 0.901$ is largely due to including wing thickness since there are no supersonic points in the flow at this condition. The decrease in flutter speed at $M = 0.96$ is attributed to both wing thickness and nonlinear effects since an embedded supersonic region of moderate size was detected in the wing tip region. The nonlinear CAP-TSD results at both $M = 0.901$ and 0.96 are slightly conservative in comparison with the experimental flutter speed index values. Nonetheless, the nonlinear CAP-TSD flutter results compare favorably with the experimental data, which is the first step toward validating the code for general transonic aeroelastic applications.

Concluding Remarks

A transonic unsteady aerodynamic and aeroelasticity code called CAP-TSD has been developed for application to realistic aircraft configurations. The name CAP-TSD is an acronym for Computational Aeroelasticity Program - Transonic Small Disturbance. The code permits the calculation of steady and unsteady flows about complete aircraft configurations for aeroelastic analysis in the flutter

critical transonic speed range. The CAP-TSD code uses a time-accurate approximate factorization (AF) algorithm for solution of the unsteady transonic small-disturbance equation. An overview of the code development effort was given and recent algorithm modifications were described. The algorithm modifications include: an Engquist-Osher (E-O) type-dependent switch to treat regions of supersonic flow, extension of the E-O switch for second-order spatial accuracy, nonisentropic effects to treat strong-shock cases, nonreflecting far field boundary conditions for unsteady applications, and several modifications to accelerate convergence to steady-state. Calculations were presented for several configurations including the General Dynamics one-ninth scale F-16C aircraft model to evaluate the algorithm modifications. The modifications have significantly improved the stability of the AF algorithm and the reliability of the CAP-TSD code in general.

Results were also presented from a flutter analysis of a 45° sweptback wing. The flutter boundaries from CAP-TSD (linear) were in agreement with parallel subsonic linear theory results and compared well with the experimental flutter data for subsonic and supersonic freestream Mach numbers. The preliminary nonlinear CAP-TSD flutter results also compared favorably with the experimental data which is the first step toward validating the code for general transonic aeroelastic applications.

References

¹Edwards, J. W.; and Thomas, J. L.: "Computational Methods for Unsteady Transonic Flows," AIAA Paper No. 87-0107, Presented at the AIAA 25th Aerospace Sciences Meeting, Reno, Nevada, January 12-15, 1987.

²Batina, J. T.; Seidel, D. A.; Bland, S. R.; and Bennett, R. M.: "Unsteady Transonic Flow Calculations for Realistic Aircraft Configurations," AIAA Paper No. 87-0850, Presented at the AIAA/ASME/ASCE/AHS 28th Structures, Structural Dynamics, and Materials Conference, Monterey, California, April 6-8, 1987. Also available as NASA TM 89120, March 1987.

³Bennett, R. M.; Bland, S. R.; Batina, J. T.; Gibbons, M. D.; and Mabey, D. G.: "Calculation of Steady and Unsteady Pressures on Wings at Supersonic Speeds with a Transonic Small-Disturbance Code," AIAA Paper No. 87-0851, Presented at the AIAA/ASME/ASCE/AHS 28th Structures, Structural Dynamics, and Materials Conference, Monterey, California, April 6-8, 1987.

⁴Cunningham, H. J.; Batina, J. T.; and Bennett, R. M.: "Modern Wing Flutter Analysis by Computational Fluid Dynamics Methods," ASME Paper No. 87-WA/Aero-9, Presented at the ASME Winter Annual Meeting, Boston, Massachusetts, December 13-18, 1987.

⁵Batina, J. T.: "An Efficient Algorithm for Solution of the Unsteady Transonic Small-Disturbance Equation," AIAA Paper No. 87-0109, Presented at the AIAA 25th Aerospace Sciences Meeting, Reno, Nevada, January 12-15, 1987. Also available as NASA TM 89014, December 1986.

⁶Batina, J. T.: "Unsteady Transonic Algorithm Improvements for Realistic Aircraft Applications," AIAA Paper No. 88-0105, Presented at the AIAA 26th Aerospace Sciences Meeting, Reno, Nevada, January 11-14, 1987.

⁷Batina, J. T.: "Unsteady Transonic Small-Disturbance Theory Including Entropy and Vorticity

Effects," AIAA Paper No. 88-2278, Presented at the AIAA/ASME/ASCE/AHS/ASC 29th Structures, Structural Dynamics, and Materials Conference, Williamsburg, Virginia, April 18-20, 1988.

⁸Boppe, C. W.; and Stern, M. A.: "Simulated Transonic Flows for Aircraft with Nacelles, Pylons, and Winglets," AIAA Paper No. 80-0130, Presented at the AIAA 18th Aerospace Sciences Meeting, Pasadena, California, January 14-16, 1980.

⁹Murman, E. M.: "Analysis of Embedded Shock Waves Calculated by Relaxation Methods," Proceedings of AIAA Computational Fluid Dynamics Conference, July 1973, pp. 27-40.

¹⁰Engquist, B. E.; and Osher, S. J.: "Stable and Entropy Satisfying Approximations for Transonic Flow Calculations," *Mathematics of Computation*, Vol. 34, No. 149, January 1980, pp. 45-75.

¹¹Goorjian, P. M.; Meagher, M. E.; and Van Buskirk, R.: "Monotone Implicit Algorithms for the Small-Disturbance and Full Potential Equations Applied to Transonic Flows," AIAA Paper No. 83-0371, Presented at the AIAA 21st Aerospace Sciences Meeting, Reno, Nevada, January 10-13, 1983.

¹²Goorjian, P. M.; and Van Buskirk, R. D.: "Second-Order-Accurate Spatial Differencing for the Transonic Small-Disturbance Equation," *Journal of Aircraft*, Vol. 23, November 1985, pp. 1693-1699.

¹³Steinhoff, J.; and Jameson, A.: "Multiple Solutions of the Transonic Potential Flow Equation," AIAA Paper No. 81-1019, Presented at the AIAA 5th Computational Fluid Dynamics Conference, Palo Alto, California, June 1981.

¹⁴Williams, M. H.; Bland, S. R.; and Edwards, J. W.: "Flow Instabilities in Transonic Small Disturbance Theory," *AIAA Journal*, Vol. 23, October 1985, pp. 1491-1496.

¹⁵Klopfer, G. H.; and Nixon D.: "Nonisentropic Potential Formulation for Transonic Flows," *AIAA Journal*, Vol. 22, June 1984, pp. 770-776.

¹⁶Hafez, M.; and Lovell, D.: "Entropy and Vorticity Corrections for Transonic Flows," AIAA Paper No. 83-1926, July 1983.

¹⁷Fuglsang, D. F.; and Williams, M. H.: "Non-Isentropic Unsteady Transonic Small Disturbance Theory," AIAA Paper No. 85-0600, Presented at the AIAA/ASME/ASCE/AHS 26th Structures, Structural Dynamics, and Materials Conference, Orlando, Florida, April 15-17, 1985.

¹⁸Gibbons, M. D.; Whitlow, W., Jr.; and Williams, M. H.: "Nonisentropic Unsteady Three Dimensional Small Disturbance Potential Theory," AIAA Paper No. 86-0863, Presented at the AIAA/ASME/ASCE/AHS 27th Structures, Structural Dynamics, and Materials Conference, San Antonio, Texas, May 19-21, 1986.

¹⁹Grossman, B.: "The Computation of Inviscid Rotational Gasdynamic Flows Using an Alternate Velocity Decomposition," AIAA Paper No. 83-1900, 1983.

20Dang, T. Q.; and Chen, L. T.: "An Euler Correction Method for Two- and Three-Dimensional Transonic Flows," AIAA Paper No. 87-0522, January 1987.

21Clebsch, A.: "Über die Integration der hydrodynamischen Gleichungen," J. Reine Angew. Math., Vol. 57, 1859, pp. 1-10.

22Fuglsang, D. F.: "Non-Isentropic Unsteady Transonic Small-Disturbance Theory," M.S. Thesis, Purdue University, West Lafayette, Indiana, May 1985.

23Whitlow, W., Jr.: "Characteristic Boundary Conditions for Three-Dimensional Transonic Unsteady Aerodynamics," NASA TM 86292, October 1984.

24Edwards, J. W.; Bennett, R. M.; Whitlow, W., Jr.; and Seidel, D. A.: "Time-Marching Transonic Flutter Solutions Including Angle-of-Attack Effects," Journal of Aircraft, vol. 20, no. 11, November 1983, pp. 899-906.

25Edwards, J. W.; Bennett, R. M.; Whitlow, W., Jr.; and Seidel, D. A.: "Time-Marching Transonic Flutter Solutions Including Angle-of-Attack Effects," AIAA Paper No. 82-3685, Presented at the AIAA/ASME/ASCE/AHS 23rd Structures, Structural Dynamics, and Materials Conference, New Orleans, Louisiana, May 10-12, 1982.

26Bland, S. R.: "Development of Low-Frequency Kernel-Function Aerodynamics for Comparison with Time-Dependent Finite-Difference Methods," NASA TM 83283, May 1982.

27Mohr, R. W.; Batina, J. T.; and Yang, T. Y.: "Mach Number Effects on Transonic Aeroelastic Forces and Flutter Characteristics," AIAA Paper No. 88-2304, Presented at the AIAA/ASME/ASCE/AHS/ASC 29th Structures, Structural Dynamics, and Materials Conference, Williamsburg, Virginia, April 18-20, 1988.

28Tijdeman, H.; Van Nunen, J. W. G.; Kraan, A. N.; Persoon, A. J.; Poestkoke, R.; Roos, R.; Schippers, P.; and Siebert, C. M.: "Transonic Wind Tunnel Tests on an Oscillating Wing with External Stores," AFFDL-TR-78-194, December 1978.

29Schmitt, V.; and Charpin, F.: "Pressure Distributions on the ONERA M6 Wing at Transonic Mach Numbers," Appendix B1 in AGARD-AR-138, "Experimental Data Base for Computer Program Assessment," May 1979.

30Yoshihara, H.: "Test Cases for Inviscid Flow Field Methods," AGARD-AR-211, May 1985.

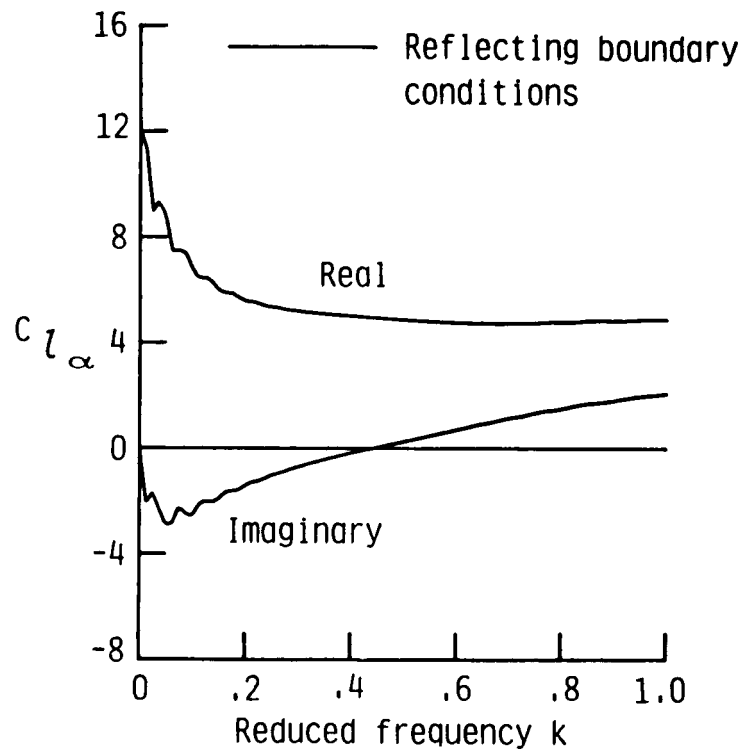
31Fox, M. C.; and Feldman, C. S.: "Model and Test Information Report, 1/9-Scale F-16C and F-16D Force and Loads Model," General Dynamics Report 16PR2179, January 1982.

32Feldman, C. S.: "Wind Tunnel Data Report, 1/9-Scale F-16C Pressure Loads Test," General Dynamics Report 16PR2252, July 1982.

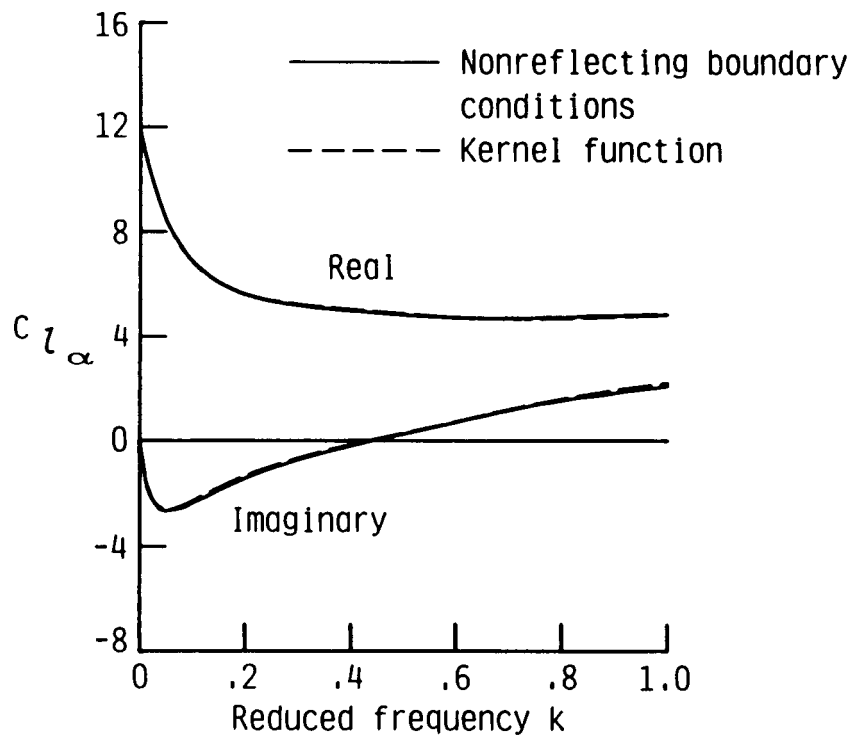
33Yates, E. C., Jr.: "AGARD Standard Aeroelastic Configurations for Dynamic Response. Candidate Configuration 1. - Wing 445.6," NASA TM 100492, August 1987.

³⁴Yates, E. C., Jr.; Land, N. S.; and Foughner, J. T., Jr.: "Measured and Calculated Subsonic and Transonic Flutter Characteristics of a 45° Sweptback Wing Planform in Air and in Freon-12 in the Langley Transonic Dynamics Tunnel," NASA TN D-1616, March 1963.

³⁵Desmarais, R. N.; and Bennett, R. M.: "User's Guide for a Modular Flutter Analysis Software System (FAST Version 1.0)," NASA TM 78720, May 1978.

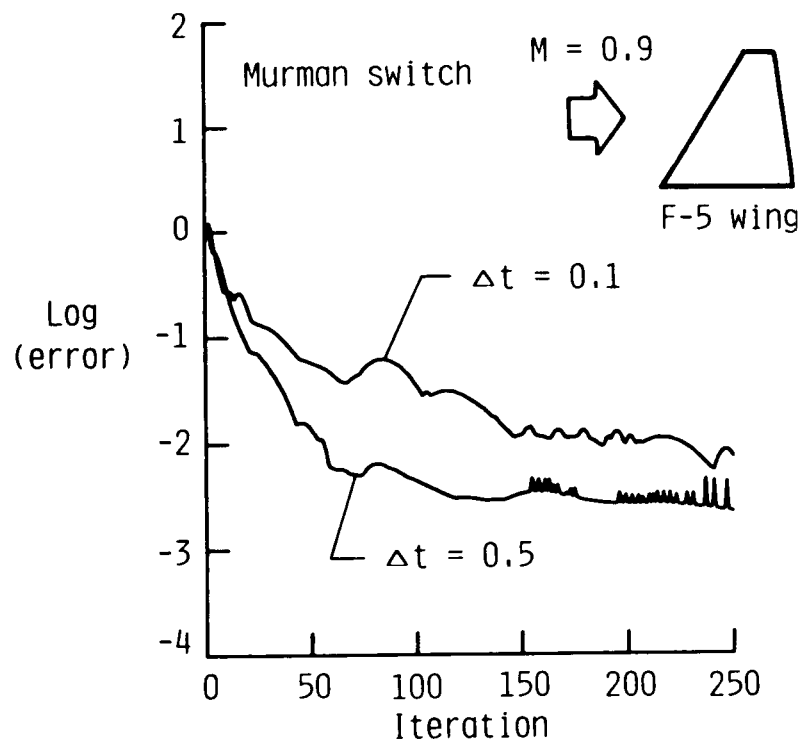


(a) reflecting boundary conditions.

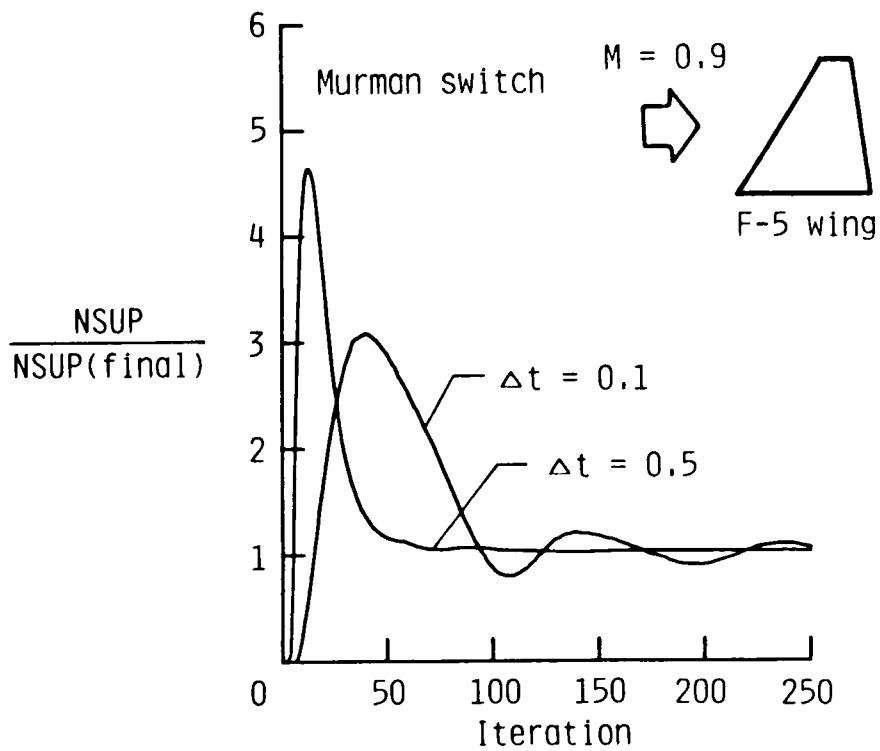


(b) nonreflecting boundary conditions.

Fig. 1 Comparisons of unsteady lift-curve slope for a flat plate airfoil at $M = 0.85$.

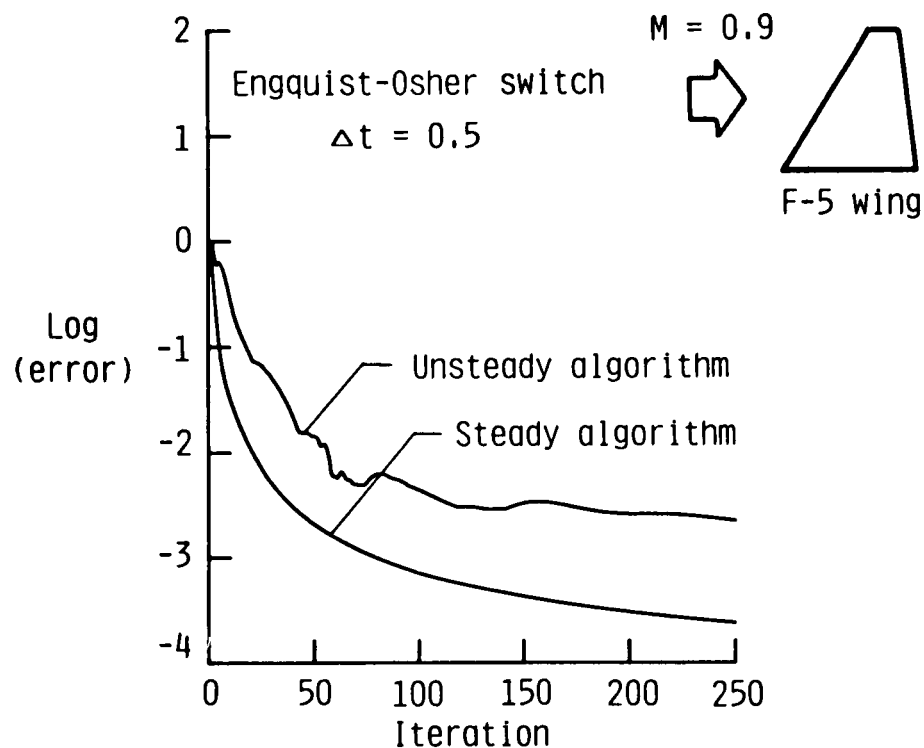


(a) steady-state convergence.

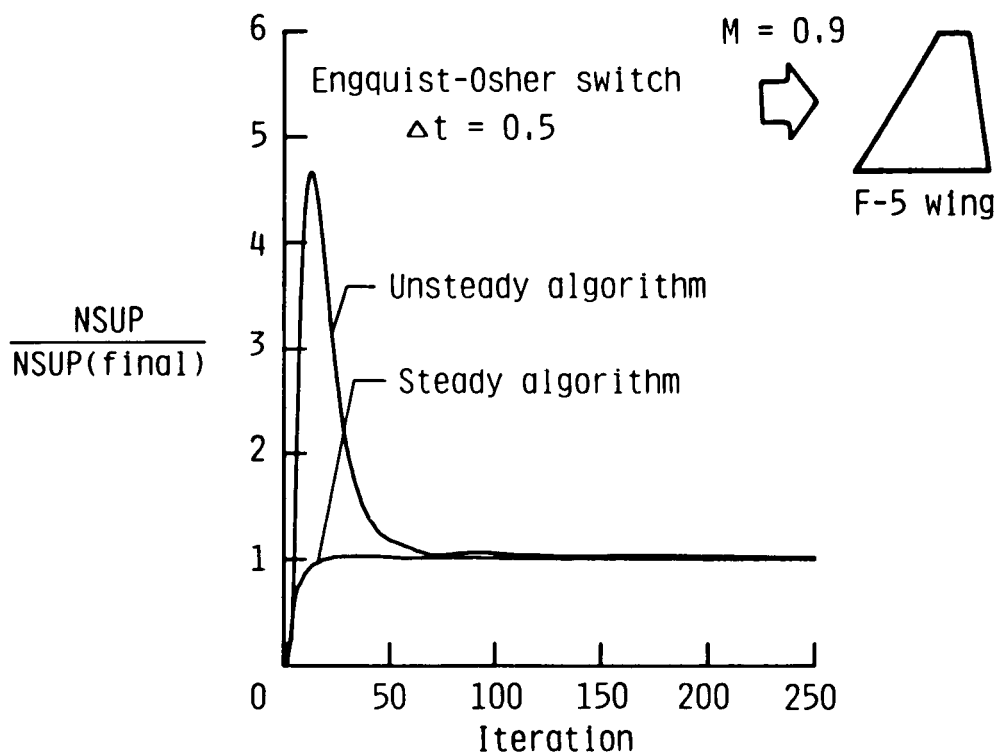


(b) number of supersonic points.

Fig. 2 Effects of step size on the solution computed using the Murman switch for the F-5 wing at $M = 0.9$ and $\alpha_0 = 0^\circ$.



(a) steady-state convergence.



(b) number of supersonic points.

Fig. 3 Effects of deleting all TSD time derivatives on the solution computed using the Engquist-Osher switch for the F-5 wing at $M = 0.9$ and $\alpha_0 = 0^\circ$.

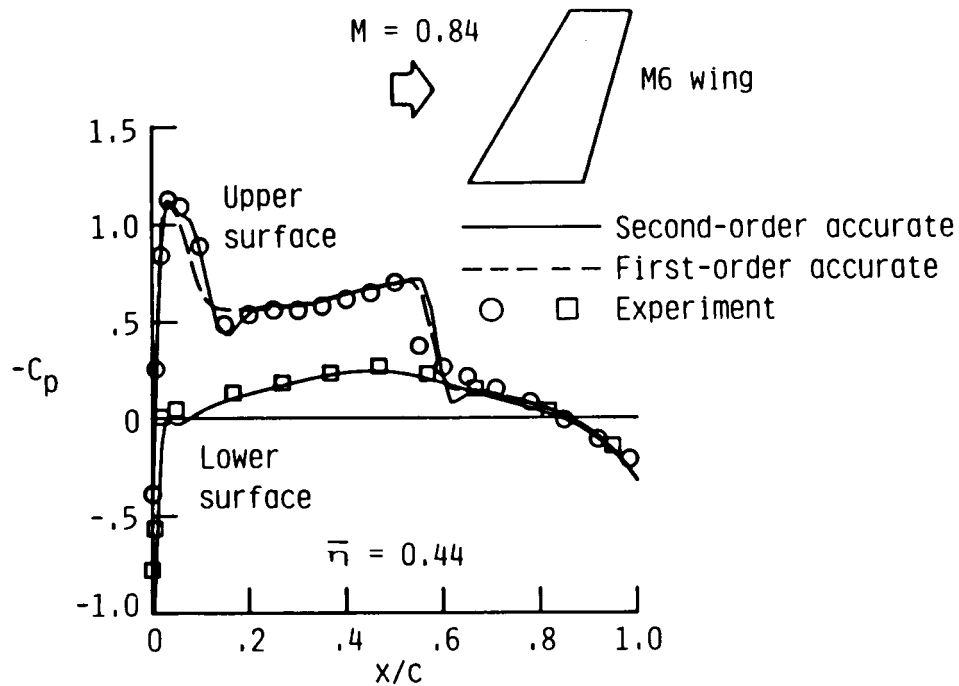


Fig. 4 Effects of first-order and second-order accurate supersonic differencing on the steady pressure distributions of the ONERA M6 wing at $M = 0.84$ and $\alpha_o = 3.06^\circ$.

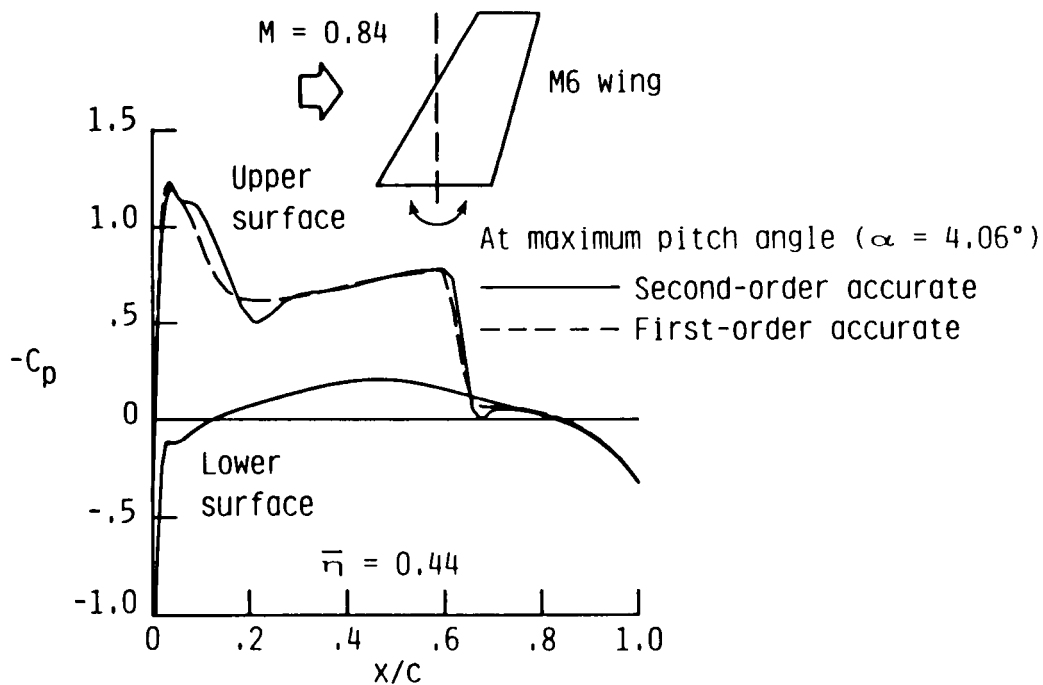


Fig. 5 Effects of first-order and second-order accurate supersonic differencing on the unsteady pressure distributions of the ONERA M6 wing during the third cycle of rigid pitching at $M = 0.84$, $\alpha_o = 3.06^\circ$, $\alpha_1 = 1.0^\circ$, and $k = 0.1$.

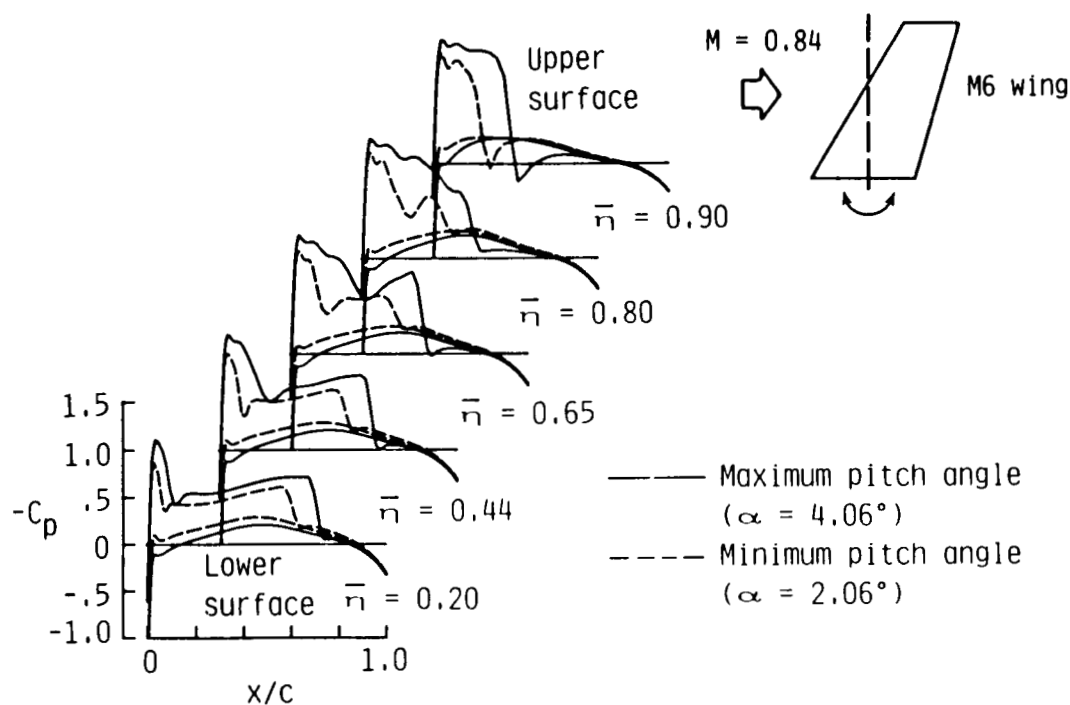


Fig. 6 Instantaneous pressure distributions on the ONERA M6 wing during the third cycle of rigid pitching at $M = 0.84$, $\alpha_0 = 3.06^\circ$, $\alpha_1 = 1.0^\circ$, and $k = 0.1$.

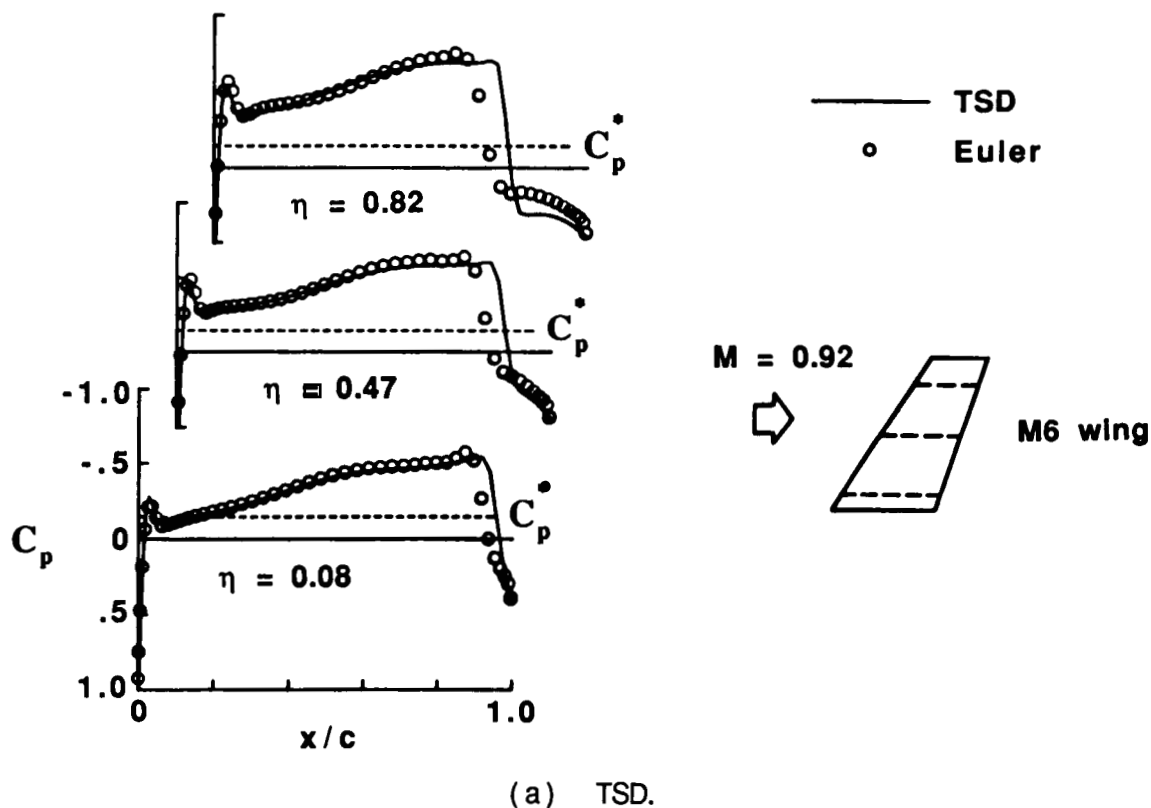
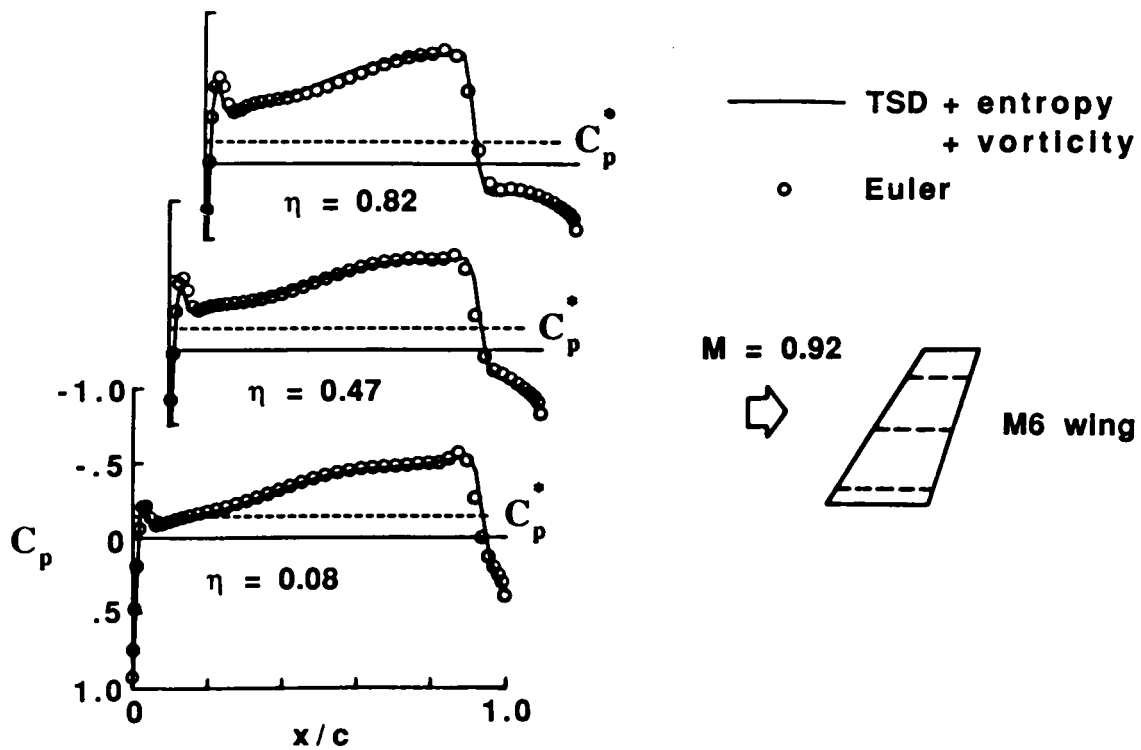


Fig. 7 Comparison of steady pressure distributions for the ONERA M6 wing at $M = 0.92$ and $\alpha_0 = 0^\circ$.



(b) TSD + entropy + vorticity.

Fig. 7 Concluded.

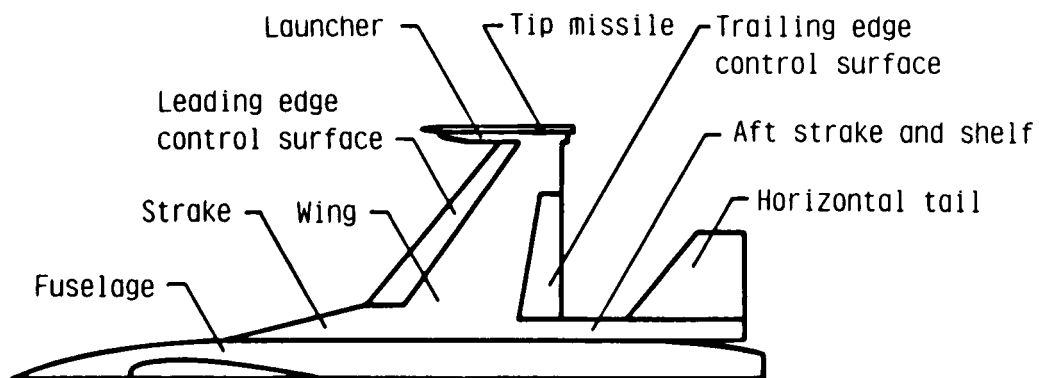


Fig. 8 CAP-TSD modeling of the General Dynamics one-ninth scale F-16C aircraft model.

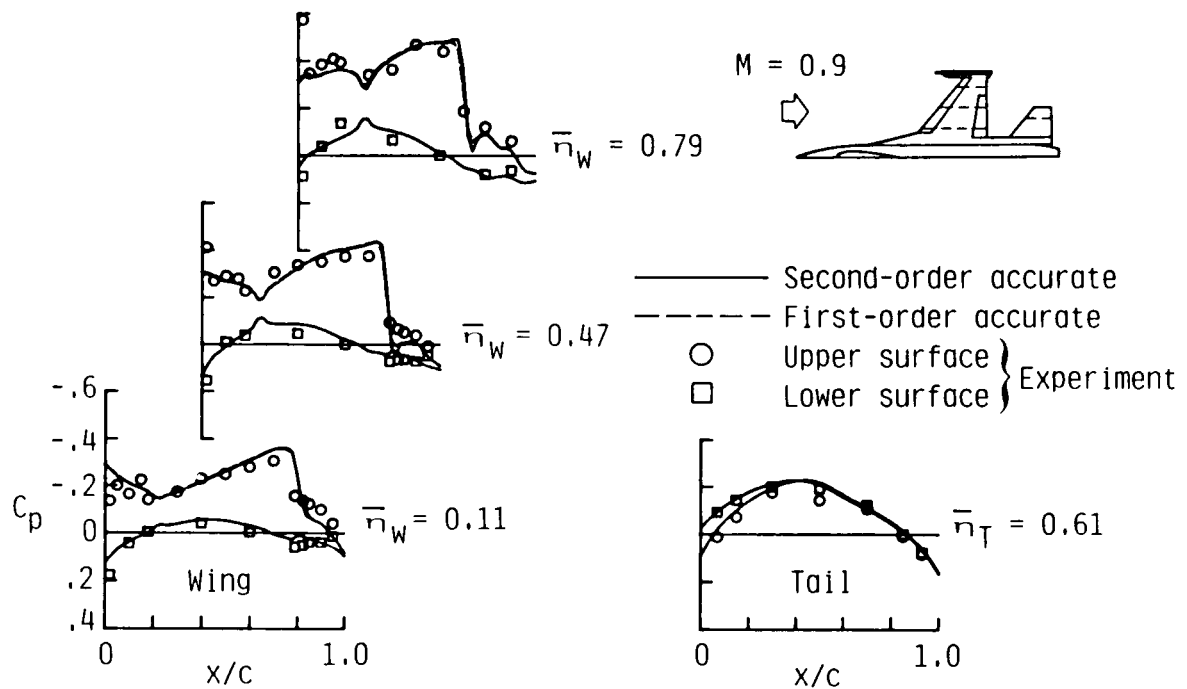
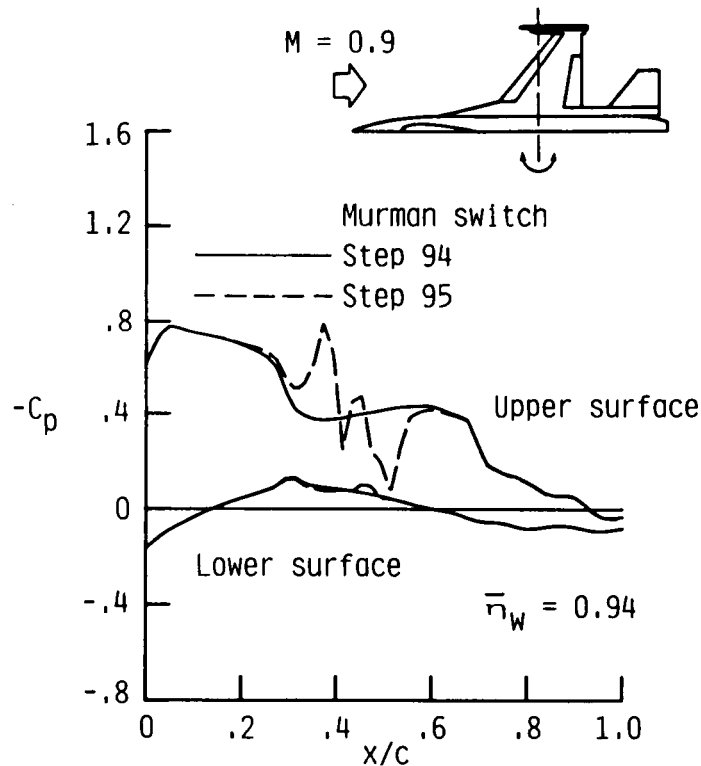
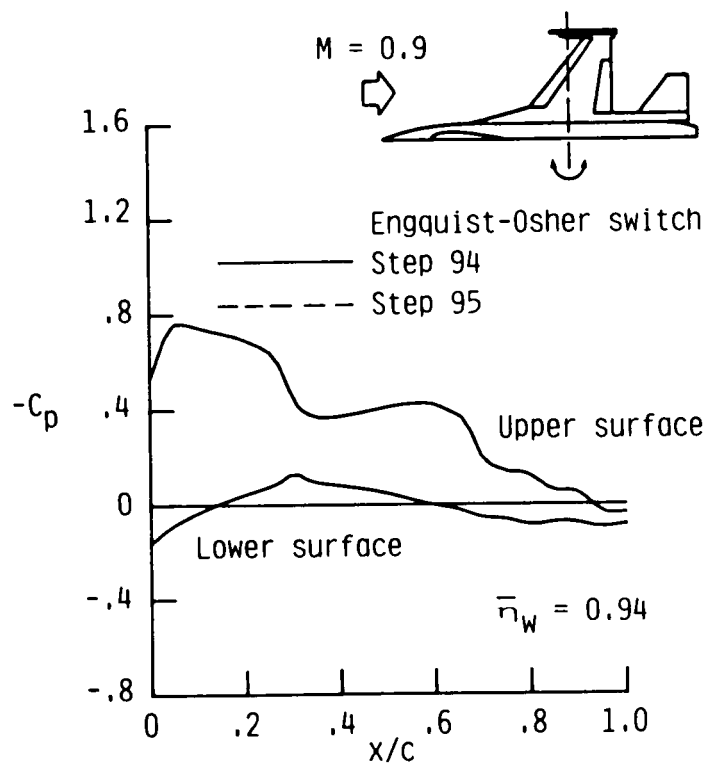


Fig. 9 Comparisons between CAP-TSD steady pressure distributions computed using first-order and second-order accurate supersonic differencing with the experimental pressure data for the wing and tail of the F-16C aircraft model at $M = 0.9$ and $\alpha_0 = 2.38^\circ$.



(a) numerical instability with Murman switch.

Fig. 10 Effect of type-dependent switch on numerical stability for rigid pitching of the F-16C aircraft model at $M = 0.9$, $\alpha_0 = 2.38^\circ$, $\alpha_1 = 1.5^\circ$, and $k = 0.1$.



(b) improved numerical stability with Engquist-Osher switch.

Fig. 10 Concluded.

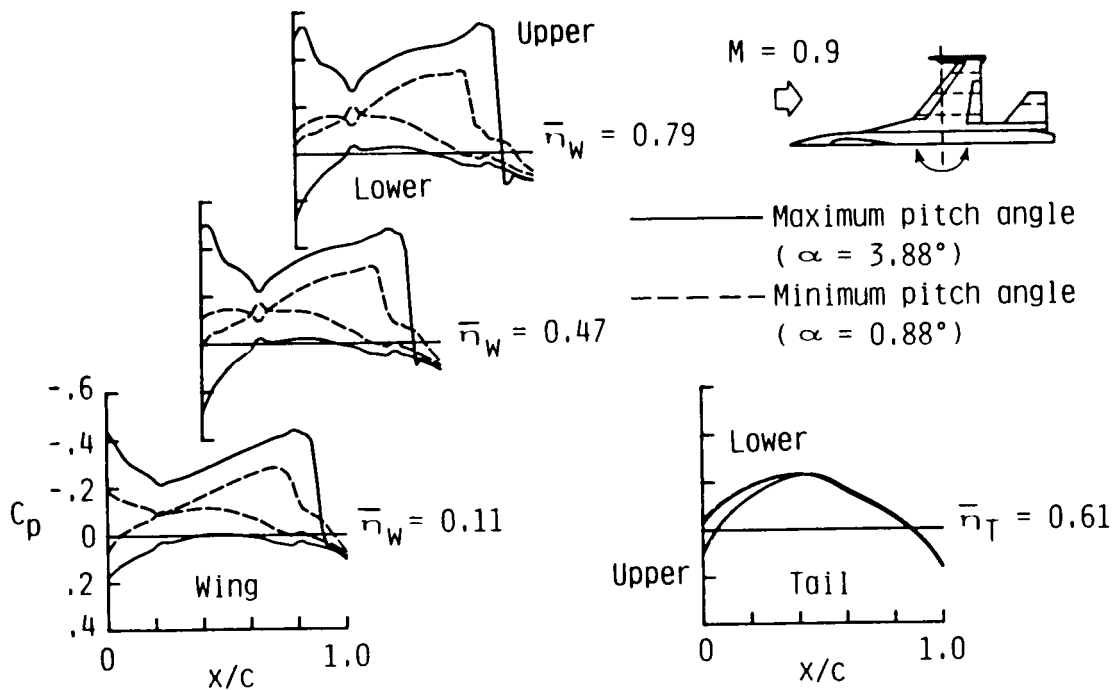


Fig. 11 Instantaneous pressure distributions on the wing and tail of the F-16C aircraft model during the third cycle of rigid pitching at $M = 0.9$, $\alpha_0 = 2.38^\circ$, $\alpha_1 = 1.5^\circ$, and $k = 0.1$.

ORIGINAL PAGE IS
OF POOR QUALITY

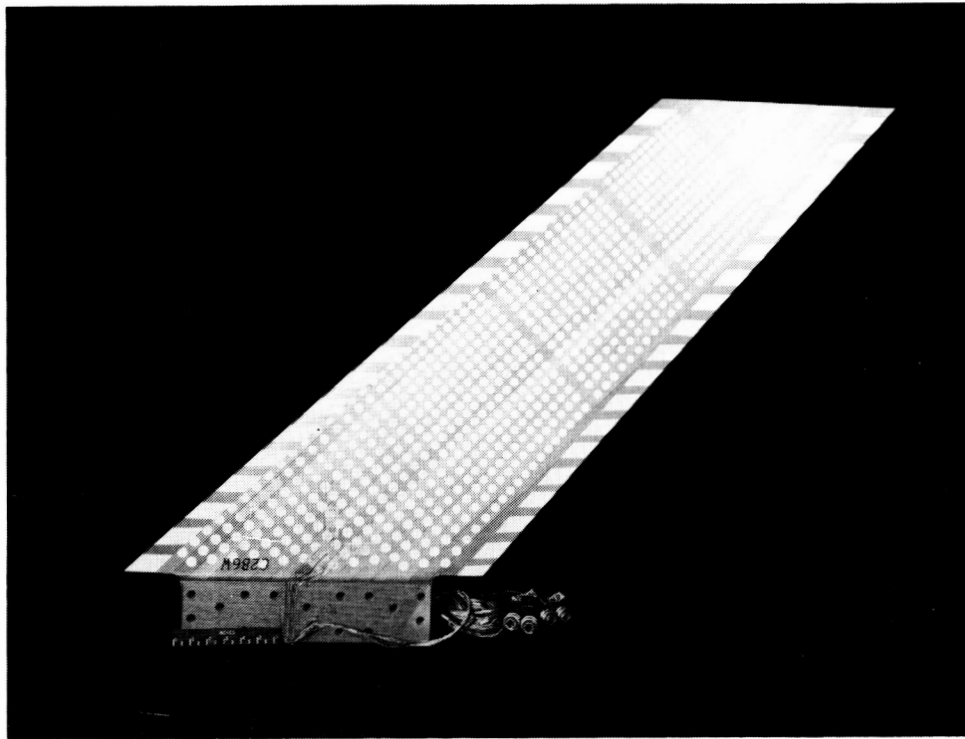


Fig. 12 Planview of 45° sweptback wing.

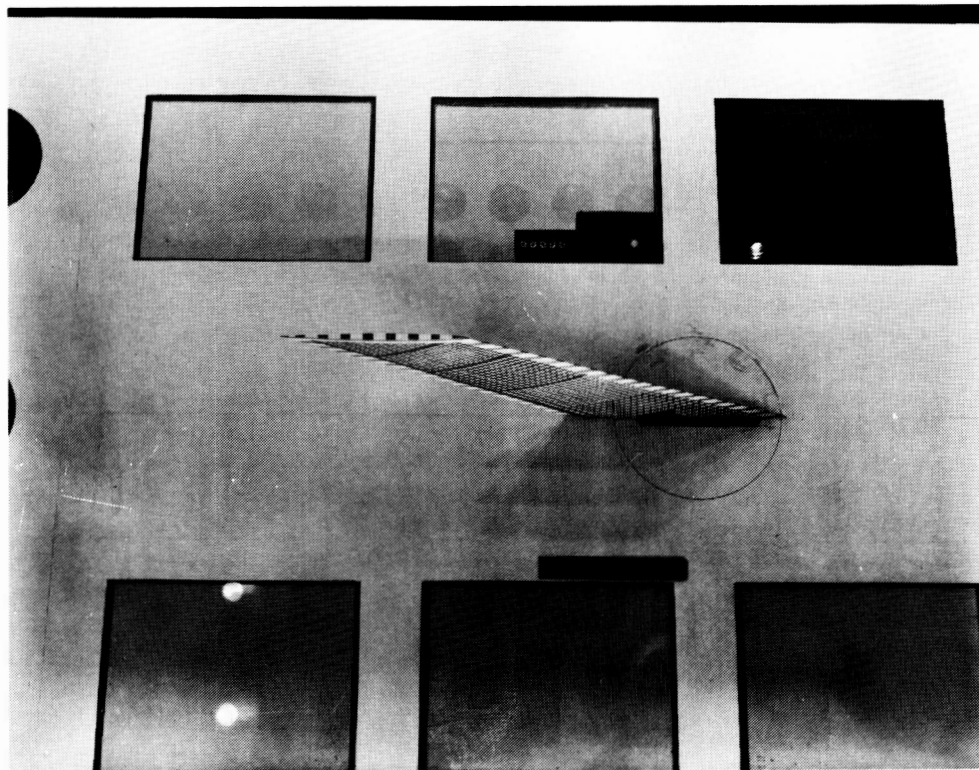


Fig. 13 45° sweptback wing in the NASA Langley Transonic Dynamics Tunnel.

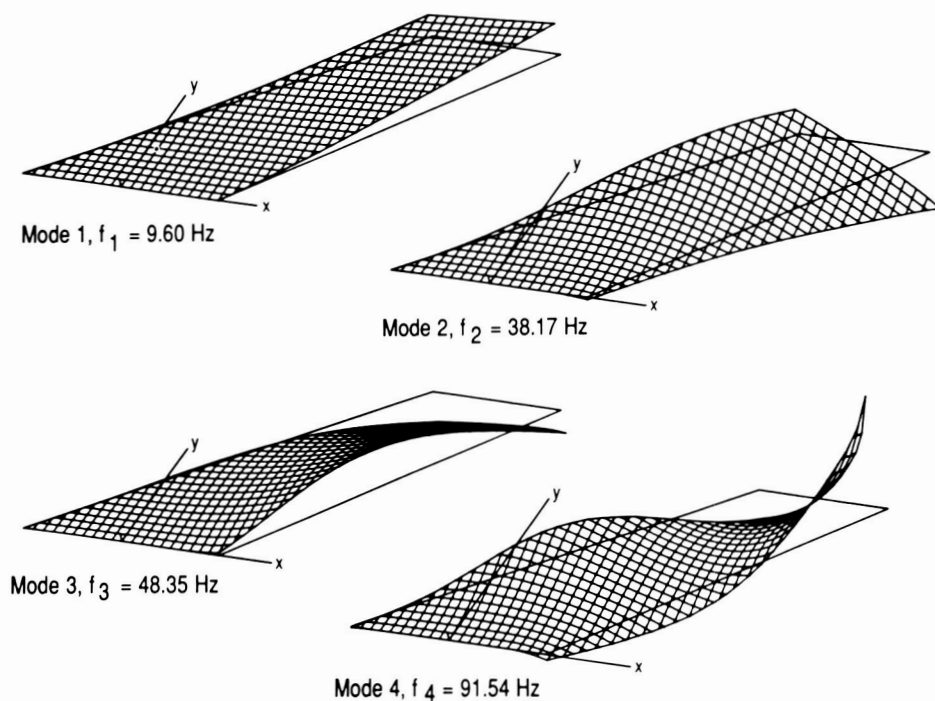


Fig. 14 Oblique projections of natural vibration modes of 45° sweptback wing.

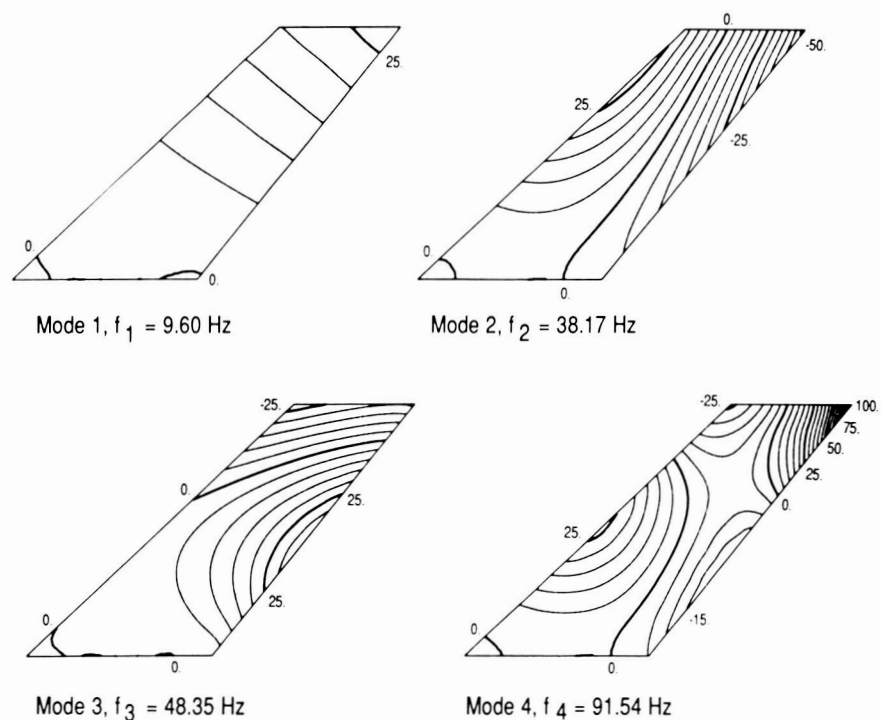
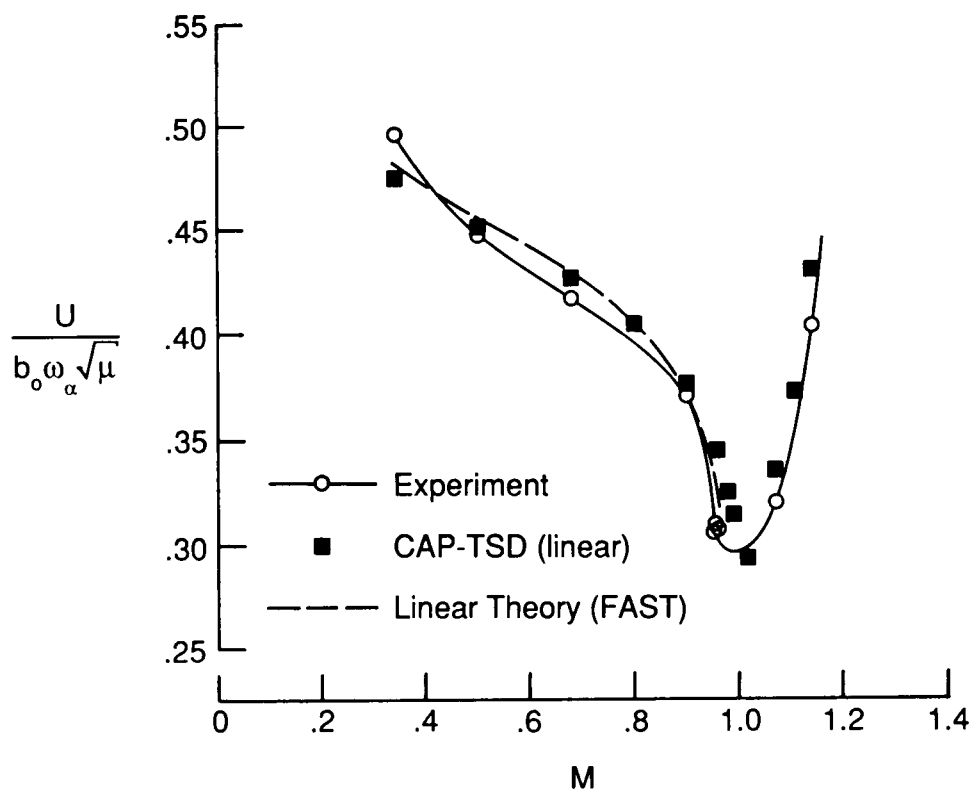
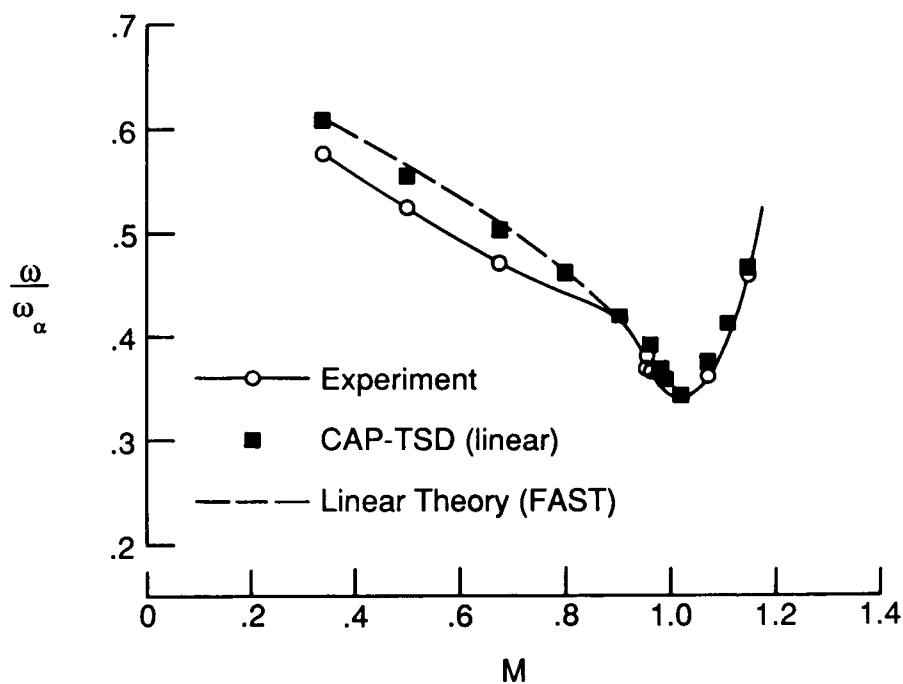


Fig. 15 Deflection contours of natural vibration modes of 45° sweptback wing.

ORIGINAL PAGE IS
OF POOR QUALITY

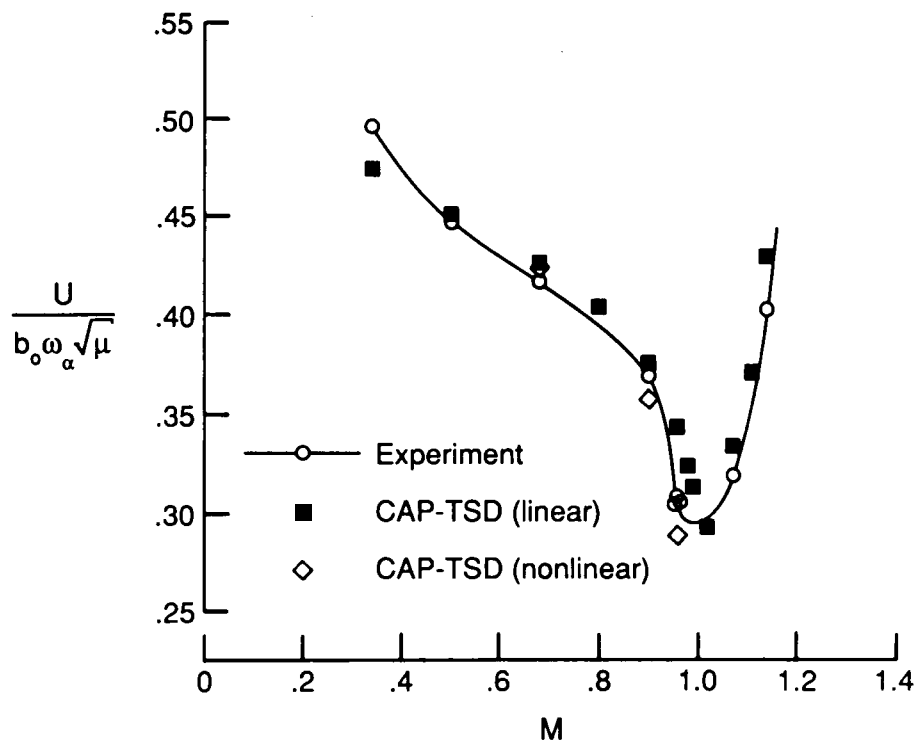


(a) flutter speed index versus Mach number.

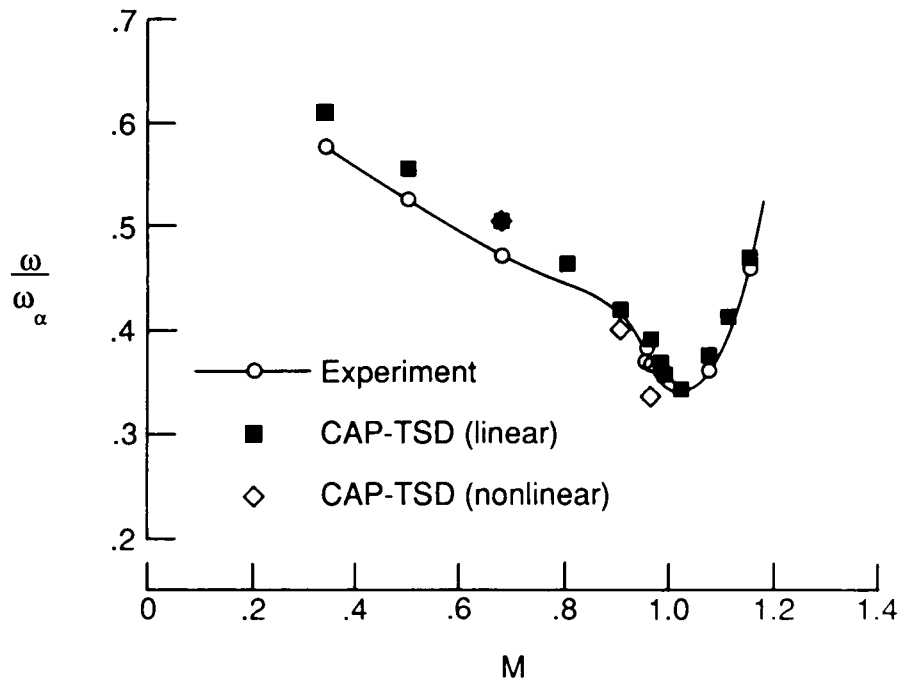


(b) nondimensional flutter frequency versus Mach number.

Fig. 16 Comparisons of linear flutter calculations with experimental data for the 45° sweptback wing.



(a) flutter speed index versus Mach number.



(b) nondimensional flutter frequency versus Mach number.

Fig. 17 Comparisons of linear and nonlinear CAP-TSD flutter predictions with experimental data for the 45° sweptback wing.